



UNIVERSITY OF LEEDS

This is a repository copy of *Fracture aperture and fill characterization in a limestone quarry using GPR thin-layer AVA analysis*.

White Rose Research Online URL for this paper:  
<http://eprints.whiterose.ac.uk/75542/>

---

**Article:**

Kana, AA, West, LJ and Clark, RA (2013) Fracture aperture and fill characterization in a limestone quarry using GPR thin-layer AVA analysis. *Near Surface Geophysics*, 11 (3). pp. 293-305. ISSN 1873-0604

<https://doi.org/10.3997/1873-0604.2012066>

---

**Reuse**

Unless indicated otherwise, fulltext items are protected by copyright with all rights reserved. The copyright exception in section 29 of the Copyright, Designs and Patents Act 1988 allows the making of a single copy solely for the purpose of non-commercial research or private study within the limits of fair dealing. The publisher or other rights-holder may allow further reproduction and re-use of this version - refer to the White Rose Research Online record for this item. Where records identify the publisher as the copyright holder, users can verify any specific terms of use on the publisher's website.

**Takedown**

If you consider content in White Rose Research Online to be in breach of UK law, please notify us by emailing [eprints@whiterose.ac.uk](mailto:eprints@whiterose.ac.uk) including the URL of the record and the reason for the withdrawal request.



[eprints@whiterose.ac.uk](mailto:eprints@whiterose.ac.uk)  
<https://eprints.whiterose.ac.uk/>

# **Fracture Aperture And Fill Characterization In A Limestone Quarry Using GPR Thin-Layer AVA Analysis**

Aisha Kana,<sup>1</sup> L. Jared West,<sup>1</sup> and Roger A. Clark<sup>1</sup>

<sup>1</sup>School of Earth and Environment, University of Leeds, Leeds, UK

## **Abstract**

Detection and characterization of fractures is important in many engineering practices e.g. rock fall assessment, quarry rock quality determination, mine roof and tunnel stability. Fractures may provide suitable contrasts in electrical properties for detection by GPR instruments. Their ability to reflect radar waves and the dependence of this reflectivity on fracture properties (aperture and fill) makes the GPR method a promising tool for rock fracture characterization. Doing so successfully requires quantification of the reflectivity, reflection coefficient,  $R$  of individual fractures, and its variation with incidence angle (AVA) or in practice, offset. Measuring the full AVA response using Common Mid Point (CMP) surveys enables simultaneous estimation of fracture aperture and fill permittivity, difficult to achieve with Common Offset (CO) profiling which does not evaluate angle dependence. This paper reports AVA analysis carried out on CMP data acquired with 500MHz antennas over Carboniferous Limestone with horizontal bedding plane fractures in Yorkshire, United Kingdom. Using the transverse electric (TE) polarization mode, data were collected at a sampling interval of 0.05ns for offsets at 0.04m steps from 0.37m to 16.05m.

The recorded amplitude is related to the reflection coefficient but is also influenced by other factors which we eliminated by making some simplifying assumptions and amplitude corrections. We assume frequency independent electrical properties, constant antenna coupling with ground surface, constant losses associated with transmission losses through any interfaces above the target reflection for range of offsets considered and a flat homogeneous surface over which measurements are made. Amplitudes were corrected for conductive attenuation, spherical spreading and antenna patterns which we measured through transillumination surveys across limestone boulders and numerical modelling using the GprMax 3D modelling code. To constrain fracture aperture and fill permittivity, we use the least squares fit of normalized reflection coefficient curves to corrected CMP amplitudes. The

analysis allowed characterization of (bedding plane) fracture fill relative permittivity ( $\sim 7.8$ ) and aperture ( $\sim 0.043\text{m}$ ,  $\sim 0.2\lambda$  at  $500\text{MHz}$ ). The values obtained are consistent with field observations of fracture fill, corresponding to a mixture of clays and calcite.

## Introduction

Fractures occur in most rocks and because they provide pathways for fluid flow, they have important implications in various practices e.g. hydrogeology, hydrocarbon exploration and engineering. Economically important hydrocarbon and water reservoirs are found in fractured rocks. These resources are produced and extracted through fractures. Where present, permeable and interconnected, they serve as conduits for fluid flow. Fracture permeability in turn depends on fracture aperture and fill. The need for detection and characterization of fractures therefore arises. Because they represent zones of anomalous electrical properties in an otherwise homogeneous host rock, the GPR method has been successfully used to identify the presence of fractures in the subsurface (e.g. Grasmuek, 1996, Theune et al, 2006). Lane et al, (1999) made an attempt to distinguish reflections from water, air or hydrocarbon filled fractures through common offset (CO) data analysis. Tsoflias et al, (2004) showed the variability of aperture along fractures from reflection amplitude analysis of CO data.

Reflections from both surfaces defining a fracture are well resolved if the aperture is larger than the dominant wavelength,  $\lambda$  of the GPR signal in the fracture. In such cases, Fresnel's coefficients (Innan and Innan, 2000) can be used to describe reflection properties for both surfaces and aperture and fill properties can then be deduced. GPR wavelengths typically fall between 0.3m and 30m in air ( $\epsilon_r = 1$ ) and 0.03 m to 3 m in water ( $\epsilon_r = 81$ ). Hydraulic apertures fall within the sub-millimetre range; e.g. Snow (1968) reported fracture widths between 100 and 200 microns within 10 m of the ground surface decreasing to between 50 and 100 microns at 100 m. These he estimated from hydraulic conductivity of fractures determined through well pressure tests. Other published hydraulic apertures include: 25 microns (Wilson and Witherspoon, 1970); 300 microns (Noorishad and others, 1971); all

cited in Nelson (2001). These apertures relate to shallow depths (hundreds of meters) and may become significantly smaller at greater depths (thousands of meters) (Nelson, 2001). Mechanical apertures, which are typically measured with GPR, can be up to 7 times wider than hydraulic apertures (Priest, 1993). Fractures therefore, have apertures less than  $\lambda$  at the dominant frequency of the GPR signal and as such generate complex reflectivity patterns as a result of interference from multiple reflections from their surfaces (**figure 1**). In order to characterize reflectivity of such fractures, thin bed analysis is necessary (Bradford and Deeds, 2006). GPR thin bed reflectivity is sensitive to host media properties (dielectric permittivity, electrical conductivity and magnetic permeability), signal characteristics (frequency, polarization and angle of incidence) and also depends on the thin bed properties i.e. aperture and fill (Hollender and Tillard, 1998, Innan and Innan, 2000, Bradford and Deeds, 2006, Deparis and Garambois, 2009). The sensitivity of thin bed reflectivity has been explored e.g. to explore frequency dependence of thin bed reflectivity, an inversion method based on analysis of the frequency content of GPR reflection was developed by Gregoire (2001) in order to characterize thin interfaces and layers. The method is based on a comparison between a measured normal incidence reflection coefficient and a synthetic one. Field reflection coefficients are calculated using a reference signal. Gregoire and Halluex (2002) applied this method to CO data in order to estimate aperture of open fractures (in the range of 3mm to 50mm) in a salt (potash) mine.

Amplitude variation with offset (hence, incidence angle, AVA) analysis involves studying reflectivity as a function of offset in order to characterize layers and interfaces. The method has been successfully applied widely to seismic data in associating contrasts in elastic properties of media with the presence of oil and gas (e.g. Ostrander, 1984, Castagna, 1993). Applying AVA analysis to GPR data was first suggested by Baker et al, (1995). For single interfaces, several authors have successfully carried out GPR AVA analysis based on the

Fresnel's reflection coefficients. Baker (1998) showed through analytical and numerical modelling that anomalous zones producing indistinguishable bistatic GPR responses (e.g. bright or dim spots in CO sections) can show very different behaviour when examined by AVA analysis. Carcione et al, (2006) studied synthetic AVA curves for various contrasts in EM properties; they highlighted the potential of AVA analysis for characterizing non aqueous phase liquid (NAPL) contamination considering a single interface between an uncontaminated upper layer and a lower layer contaminated with LNAPL. Applying the analysis to GPR data, Deeds and Bradford (2002) successfully characterized the presence of an NAPL contaminated zone at an alluvium/clay boundary. Bradford and Deeds (2006) investigated the AVA response of a thin bed and proposed a validity limit of the standard Fresnel's equations in describing thin bed reflectivity, as that where the bed thickness is less than 0.75 times the dominant GPR  $\lambda$  in the thin bed. They further analyzed AVA curves using an analytical solution to the thin bed reflectivity and successfully applied their thin bed model in identifying a thin NAPL contaminated layer in the saturated zone. Successful application of thin bed AVA analysis in characterizing hydrocarbon contamination in the subsurface suggests the method can be extended to subsurface fracture characterization as both targets are similar i.e. thin beds (Bradford and Deeds, 2006). Deparis and Garambois (2009) studied dispersive frequency dependent amplitude and phase variation with offset (APVO) curves for a restricted case of a thin bed embedded within a homogeneous rock and assessed its potential for characterizing the aperture and fill of such layers. Their approach to estimating thin bed aperture and fill is an inversion scheme which compares in the frequency domain, field data with synthetic data generated from analytical solutions to thin bed reflection coefficients. They applied the methodology to CMP data acquired over a vertical fracture on a cliff face and successfully characterized the aperture (0.04m) and fill permittivity (3.1).

In previous applications to fracture characterization, AVO analysis has not been applied to thin fracture such as typically encountered in the subsurface. This paper reports on thin fracture aperture and fill permittivity characterization in a limestone quarry using AVA analysis. The analysis considers the case where the host rock is not homogeneous i.e. rock above and below the fracture have different electrical properties and is based on EM plane wave reflection theory for a three layer system derived by King and Owens (1992) and presented in Bradford and Deeds (2006). The reflectivity in this case is a composite of two reflections: one which will result if there was no fracture and an interference product of reflections from the surfaces defining the fracture (Widess, 1973). We consider very thin fractures ( $\sim 0.25\lambda$ ) typical of this field site as observed on quarry walls; apertures are typically less than 0.04m. We initially study the reflectivity sensitivity to incidence angle (AVA behaviour), fracture aperture, and fill permittivity, by computing theoretical reflection coefficients. Using the broadband model presented in Bradford and Deeds (2006), normalized reflection amplitudes versus incidence angle were computed for thin fractures in limestone. We then characterize intrinsic attenuation and antenna radiation\ sensitivity patterns both necessary in order to access the 'true' AVA response. Composite antenna patterns were measured from field surveys and numerical simulations; an approach which enables correcting for both transmitter radiation pattern and receiver sensitivity. Intrinsic attenuation was estimated from  $Q^*$  extracted from CMP data through spectral ratios analysis. Finally, we apply these corrections to CMP data acquired along the quarry floor for a bedding plane fracture. To constrain fracture aperture and fill permittivity, we use a least squares fit to fit normalized reflection coefficient curves (defined by sets of fracture apertures and fill) to corrected CMP amplitudes. The analysis highlights the potential of the AVA method in constraining fracture properties. **Figure 2** is a flow chart summarising the practical approach to fracture AVA analysis, as reported in this paper.

## Field site characterization

### Location and Geology

Field surveys were conducted in a former quarry, Threshfield near Grassington in Yorkshire, United Kingdom. Solid geology in the site (figure 3a) consists of Carboniferous limestone, in particular the Great Scar Limestone group including the Gordale and Cove formations, seen in the quarry and the Kilnsey Formation which outcrops to the far northwest of the quarry. According to Hafren Water (2003), boreholes drilled within the quarry boundaries prove an upper sequence of light grey, well bedded strong limestone, which are the Gordale and Cove Formations; it is believed that the Kilnsey Limestone lies just beneath the Cove Limestone followed by the Kilnsey Limestone With Mudstone (figure 3b).

### Fracture aperture and fill

Discontinuity surveys along quarry walls show that the rock is well fractured with sub-vertical joints and sub horizontal bedding plane fractures. The walls were sampled in windows of at least 4m<sup>2</sup> in area; fracture aperture and fill characteristics were observed. We acknowledge that being a free surface, that data collected along quarry walls, may not be truly representative of subsurface characteristics due to stress relief, blasting damage and degradation due to weathering. However, an insight into fracture characteristics will be gained. Apertures are predominantly less than 40mm (figures 4a and 4b).

Open fractures contain, predominantly, a fine grained clayey infill; samples were analysed using a scanning electron microscope (SEM) and x-ray diffraction (XRD) in order to characterize the mineralogy (see **figures 5a and 5b**). SEM results show the presence of clay minerals in all samples; calcite was also seen, in addition to large grains of quartz and barite. The XRD result is shown in figure **5b** for one sample; muscovite and kaolinite were

seen in all samples; calcite in most samples; and anatase, quartz, microcline feldspar and barite in some samples (figures 5a and 5b).

Based on its composition, electrical properties of the fracture fill will differ from the host limestone. Although calcite will have similar properties to the limestone, presence of other materials and porosity in the fill will influence the properties especially if wet. Dielectric permittivity will be between 3 and 5 if dry and between 8 and 40 if wet corresponding to values for a mixture of sands (dry, Reynolds, 1997; and wet, West et al, 2003) calcite (Reynolds, 1997) and clays (Davis and Annan, 1989). Given these properties, water saturated fractures form excellent targets for GPR surveys in the field site although dry fractures will be less visible given that host rock permittivity is 8 (Reynolds, 1997). Secondly, high resistivity (low conductivity) of the limestone will allow reasonable penetration of high frequency GPR waves which is necessary in order to maximize resolution. Also, the gently dipping bedding planes facilitate CMP surveys and subsequent AVA analysis.

## **AVA analysis**

### **Overview**

AVA analysis involves studying the variation of reflection amplitude with offset (and corresponding incidence angles) in order to characterize some geophysical property contrasts across an interface (e.g. Lehman, 1996, Baker, 1998). It is a form of attribute analysis with the main aim of relating amplitude variations in wave forms (e.g. amplitude, phase and frequency content) to physical properties of the propagating media; although most AVA analyses do not consider phase and frequency dependence instead, this dependence is accounted for: e.g. by Bradford and Deeds (2006) where envelope or Hilbert transform amplitudes (Sheriff, 2002) are considered. Conventional GPR data are collected with a

constant antenna separation/offset (CO), but for AVA analysis, GPR data must be collected using the common midpoint (CMP) survey geometry. In the CMP mode, antennas are moved symmetrically about a midpoint increasing the offset, and data collected for the same point on a reflector (assuming a horizontal interface) so that the reflections are recorded for each antenna offset. The antenna offset is subsequently converted to angle of incidence taking into account radar velocity in the overburden above the target reflector. A plot of reflection amplitudes against the angle of incidence represents the main diagnostic data for the analysis (Castagna, 1993, Baker, 1998). There are, however, other factors which need to be considered in carrying out the CMP surveys and subsequent AVA analysis. Acquisition considerations have been discussed in Bradford (1998) and Bradford and Deeds (2006); they mainly concern collecting sufficiently long offsets to observe the AVA effect; this depends target reflector depth any velocity variation in the overburden. Furthermore, the reflection amplitude recorded is influenced by other factors unrelated the fracture including: the source amplitude ( $A_{sou}$  (mV)); geometric spreading (S); intrinsic attenuation in the propagating medium ( $\exp(-\alpha r)$ ); antenna (transmitter and receiver) pattern ( $P_{TR}$ ) and antenna coupling with the ground surface ( $C_{TR}$ ) and transmission losses (t) across interfaces above the reflecting interface. The recorded amplitude ( $A_{obs}$  (mV)) can be expressed as:

$$A_{obs} = A_{sou} \cdot \frac{C_{TR} \cdot P_{TR} \cdot t}{S} \cdot R \cdot \exp(-\alpha r) \quad (1)$$

Where:  $\alpha$  ( $m^{-1}$ ) is the attenuation coefficient and  $r$  (m) is the ray path length. R is the absolute reflection coefficient.

The factors listed above depend on the ray path geometry and frequency dependent media properties (permittivity, conductivity and magnetic permeability) and on signal characteristics such as frequency and polarization of the propagating radar wave. These factors are outlined in Castagna (1993) and explained in Bradford and Deeds (2006) for the GPR case.

For the following analysis, assumptions made include: frequency independent electrical properties (and hence velocity) which is reasonable for effective propagation within the bandwidth of the GPR signal through most materials (Annan, 1996). Others are constant antenna coupling with ground surface, and constant transmission losses for range of offsets considered. To justify the latter assumptions, the surface over which measurements are made must be uniform with a homogeneous surface material, and strata in the overburden must be horizontal and parallel to the ground surface. The surface over which our CMP data were collected is indeed relatively flat. Bradford and Deeds (2006) conclude that errors associated with assuming constant transmission losses are less than 5% for incidence angles up to 65% of the critical angle for increasing velocity with depth. For decreasing velocity with depth, the assumption is valid for incidence angles from 35° to 55°. Information on the absolute source amplitude is also difficult to obtain, it is therefore necessary to normalize the observed amplitudes e.g. by a near offset amplitude or maximum amplitude. The reflection amplitude ratio can be written as:

$$\frac{A_{obs}(\theta)}{A_{obs}(\theta=0)} = \frac{R_{\theta} \cdot P_{TR\theta} \cdot S_{\theta=0}}{R_{\theta=0} \cdot P_{TR(\theta=0)} \cdot S_{\theta}} \cdot \exp^{-\alpha(r_{\theta}-r_{\theta=0})} \quad (2)$$

By correcting for antenna pattern, geometric spreading and intrinsic attenuation (**figure 2**), the normalized amplitude at a given angle of incidence approximates the normalized reflection coefficient R i.e.:

$$\frac{A_{corr\theta}}{A_{corr\theta=0}} = \frac{R_{\theta}}{R_{\theta=0}} \quad (3)$$

The resulting normalized reflection amplitudes can then be compared with normalized theoretical amplitudes in order to constrain interface and layer properties. For the whole analysis presented below, we consider only transverse electric (TE) mode data and unless

otherwise stated, amplitude is defined as the local maximum of the envelope function (Sheriff, 2002) for the duration of the GPR wavelet.

### Theoretical computations of $R$ curves

Fresnel's reflection coefficients  $R$  (Innan and Innan, 2000) quantify the amount of incident electromagnetic (EM) wave amplitude reflected at an interface separating two media of contrasting EM properties.  $R$  depends on the dielectric permittivity of the media through which the radar wave is propagating, angle of incidence and polarization of the incident EM wave. Assumptions include uniform plane waves propagating in homogeneous and isotropic media with frequency independent properties; magnetic permeability is equal to that of free space and both media are semi-infinite in extent. Fresnel's equations also assume planar interfaces and give the AVA response of a single interface.

Fresnel's equations are however invalid for such targets as thin beds with thicknesses less than  $0.75\lambda$  (Bradford and Deeds, 2006) where frequency dependent constructive and destructive interference occurs between multiple reflections from top and bottom of the thin bed, leading to complex reflectivity patterns. An analytic solution to thin bed AVA is the multi-layer EM plane wave reflection coefficients derived by King and Owens (1992) and reduced to that for a three-layer sequence by Bradford and Deeds (2006), equation 4. Equation 4 considers a system comprising an upper and lower half space (layers 1&3) separated by a layer (layer 2) of finite thickness ( $h_2$ ) (**figure 1**). The reflection coefficient in TE mode,

$$R_{TE} = \frac{\gamma_1 - \gamma_3 - i\left(\frac{\gamma_1\gamma_3}{\gamma_2} - \gamma_2\right)\tan(\gamma_2 h_2)}{\gamma_1 + \gamma_3 - i\left(\frac{\gamma_1\gamma_3}{\gamma_2} + \gamma_2\right)\tan(\gamma_2 h_2)}, \quad (4)$$

$$\gamma_n = \omega\sqrt{\varepsilon_n\mu} \cos \theta_n ,$$

$$\cos \theta_n = \left[1 - \frac{\varepsilon_1 \sin^2 \theta_1}{\varepsilon_n}\right]^{1/2} ,$$

where  $\varepsilon$  is dielectric permittivity,  $\theta$  is angle of incidence,  $\omega$  is angular frequency (Hz),  $\mu$  is vacuum magnetic permeability ( $1.26 \times 10^{-6}$  H/m),  $h_2$  is thickness of the thin bed (m),  $i$  is  $\sqrt{-1}$ , and  $\gamma$  is wave number. TE is transverse electric (perpendicular) polarization and subscripts 1, 2, 3 & n refer to layers 1, 2, 3 & n respectively.

A response in field data is for a broad band signal so we computed the reflected field for a broadband signal i.e. normalized AVA curves for fractures in limestone with aperture and fill characteristics observed in the field. We used the model described in Bradford and Deeds (2006) for reflectivity from the top of a three layer sequence. A source spectrum is filtered with equation 4 and the inverse Fourier transform (ifft) of the filtered spectrum gives the time domain response. In Bradford and Deeds, a Ricker wavelet was used as the source wavelet; here, we use a field - recorded wavelet with antennas put together i.e. facing each other. Broadband curves show a dependence on both fracture aperture and fill properties (figure 6). R generally increases from a minimum at normal incidence up to unity at  $\theta_1 = 90^\circ$ . Except for air filled fractures, R curve is initially flat (at low  $\theta_1$ ) and only becomes sensitive to  $\theta_1$  at  $\theta_1 > 20^\circ$ . Influence of the contrast between  $\varepsilon_1$  and  $\varepsilon_3$  (layers 1 and 3) is seen to produce a minimum rather than zero reflectivity at normal incidence and total internal reflection beyond the critical angle of incidence (in this case  $\sim 58^\circ$ ) i.e.  $\varepsilon_1 > \varepsilon_3$ . Whether the predicted dependence of R on  $\theta_1$  is enough to distinctly characterize layer properties will depend on the degree of contrast in electrical properties presented by the fractures in the field site.

### **CMP data acquisition and processing**

CMP data were acquired on the horizontal quarry floor using a PulseEkko Pro GPR system with 500MHz antennas. Antenna offsets ranged from 0.37m to 16.05m at increments of 0.04m (table 1). CMP data were processed using Reflex-Win Version 3.5.1 software (Sandmeier, 1997-2004). To preserve amplitude characteristics which are of interest, minimal

processing was applied to the data; de-wow, 250-750MHz band pass Butterworth filter and time zero corrections.

Ideally the apparent velocity of the direct air wave event on the CMP section should be the speed of light. These data initially gave a velocity of  $0.289 \pm 0.0075$  m/ns (s.e); this value underestimates the speed of light (0.3m/ns) by about 3.7%, believed to be due to shortening of recorded offsets relative to intended offsets (Barrett et al, 2007). To correct data for this error, all offsets were increased by 3.7% which is closer to the speed of light i.e.  $0.2993 \pm 0.0085$  m/ns and a corresponding time zero of  $82.043 \pm 0.1$  ns (s.e) which is closer to the speed of light. Figure 6a shows the processed CMP section including 30ns AGC gain. Data quality is good; direct air and ground waves and reflections (interpreted as the horizontal bedding plane fractures) are visible (figure 7a).

Semblance analysis was done in order to estimate a 1D velocity model and thence a permittivity model (figure 7b). Back shifting (Booth et al. 2010) was applied to semblance picks to obtain estimates of velocity as close as possible to rms velocity (corresponding to first break times) that were then converted using Dix's equation (Dix, 1955), to interval velocities ( $V_{int}$ ); layer thicknesses and depths to interfaces were then computed from the interval velocity and zero-offset times. The target for AVA analysis is reflector  $f_1$  (figure 7a). Although it is preferable to target the shallowest reflection to avoid correcting for transmission losses,  $f_1$  is more continuous with a higher signal to noise ratio than  $f_0$  and will provide wider angles for the AVA analysis. Furthermore, interval velocities above  $f_1$  are not significantly different ( $0.091 \text{ mns}^{-1} \pm 1.5 \times 10^{-5}$  and  $0.095 \text{ mns}^{-1} \pm 5.5 \times 10^{-3}$ ) respectively, hence the overburden above  $f_1$  will be treated as a single layer. The velocity model is shown in figure 7c and comprises a thin fracture ( $f_1$ ) sandwiched between an upper layer (1) and a lower layer (3) of differing electrical properties (i.e.  $\epsilon_{r1} \neq \epsilon_{r3}$ ), **see table 2**. Equivalent incidence angles are from  $9^\circ$  to  $55^\circ$  which is sufficient to observe the important AVA

characteristics. Interference from the direct ground wave and other shallower events limits accessing higher angles.

## **Amplitude corrections**

### **Antenna pattern**

GPR antennae typically show a strong directionality when used for surface surveys; this must be accounted for in AVA analysis. Analytical solutions for the radiation pattern of a dipole antenna located on a planar boundary between 2 semi-infinite media have been presented by several authors e.g. Annan et al. (1975) and Engheta et al. (1982), describe the far-field radiation pattern of an infinitesimal dipole antenna as having a sharp maximum in the TE plane at the air to ground critical angle. GPR surveys are, however, typically in the near-field, with targets usually within  $2-20\lambda$  at the dominant signal frequency (Bradford and Deeds, 2006). Near-field patterns determined experimentally and through numerical modelling differ from far-field patterns e.g. Annan et al. (1975), Holliger and Bergman, (1998), Valle et al. (2001) and Radzevicius et al. (2003). In particular, TE patterns are broader and maxima do not occur at the critical angle. For these reasons, Bradford and Deeds (2006) suggest constructing case specific antenna patterns that do not depend on the far-field approximation. They also reported that the semi-empirical radiation pattern derived by Bradford (1998) and similar to laboratory measurements of Annan et al. (1975) yielded good results when applied to AVA analysis. The semi-empirical pattern has the form  $\sec(\theta)$  at low angles of incidence and converges on the far-field pattern at higher angles of incidence. In a modelling study, validated by laboratory measurements, Radzevicius et al. (2003) showed that near-field antenna patterns result from interference between lateral and surface waves and depend on electrical properties of the ground and observation distance; the shape becomes narrower with increasing dielectric permittivity and antenna height above the

ground surface. Near-field patterns converge towards the analytical far-field pattern with increasing observation distance but a complete match is still not observed at observation distances equivalent to  $40\lambda$  at the dominant frequency (Valle et al, 2001). At 500MHz centre frequency,  $\lambda$  for our field site is in the range 0.24m to 0.19m assuming a velocity between 0.095m/ns and 0.12m/ns. At a depth of 1.19m and within the signal bandwidth (250 to 750MHz),  $f_1$  is in the near field of the antennas (observation distance  $\sim 3\lambda$  to  $6\lambda$ , velocity = 0.095 m/ns) implying that the radiation pattern will differ from the analytic pattern.

Recorded GPR amplitudes contain the composite effect of transmitter (direction in which the energy leaves the antenna) and receiver (direction in which the energy is recorded) antennae. The composite pattern can be observed in the field by measuring the variation in amplitude of the direct wave as a function of propagation direction through a homogeneous material in transillumination surveys. We test this approach through numerical modelling and field measurements.

### **Numerical simulations of antenna patterns.**

Numerical models were generated from the 3D finite difference time domain (FDTD) code GprMax (Giannopoulos, 2005). FDTD codes have been successfully used to characterize near-field GPR antenna radiation characteristics (e.g. Holliger and Bergman, 1998, Radzevicius et al. 2003, and Deparis and Garambois 2009). The FDTD approach to numerical modelling involves discretizing both space ( $\Delta x$ ,  $\Delta y$ , and  $\Delta z$ ) and time ( $\Delta t$ ) domains so that the model consists of a grid of linear, isotropic and homogeneous FDTD cells. The numerical solution is iteratively obtained in the time domain using a discretized form of Maxwell's equations which are applied in each FDTD cell. For each iteration, the electromagnetic (EM) field advances in the FDTD grid with an elapsed time  $\Delta t$  so that the number of iterations determine the total time window. For a detailed description of the code and examples, readers are referred to Giannopoulos (2005). Model geometry (figure 8a)

consists of a block of limestone ( $\epsilon_r = 9$ ) of thickness equivalent to the observation distance. The antennas are first placed on both sides of the block so that the direct wave impinges on the block edge at normal incidence; the receiver is then moved in increments equivalent to the sampling interval of the surface CMP thus increasing the radiation angle with each increment. A Hertzian dipole with a 500MHz ricker source pulse was specified. The discretization step was set to smaller than  $\lambda/10$  to reduce numerical dispersion (Giannopoulos, 2005). Conductivity was not included as it has been shown in Radzevicius et al. (2003) that this property does not affect the shape of the radiation pattern.

### **Field measurements of antenna patterns and comparison with simulated patterns**

To validate the numerical approach outlined in the previous section, transillumination surveys were conducted. A 500MHz Pulse Ekko pro GPR system was used to collect TE mode direct wave amplitude data as a function of direction through a transillumination survey across a 0.9m thick limestone block. Table 3 summarizes acquisition parameters.

Both numerical and field data were processed using Reflex-Win Version 3.5.1 software (Sandmeier, 1997-2004). Processing comprises: de-wow (field data), band pass filtering (250-750MHz) and envelope. Envelope amplitudes were corrected for non-conductive geometric spreading. In field and simulated radargrams (figures 8c & 8d), direct and lateral waves are present; in the region of interference, the two events are inseparable, beyond this they become distinct. The basic shape of the composite pattern is similar with the hump observed in both field and simulated data sets occurring in the region of interference (figure 8b). Low offset behaviour of field data may be indicative of interference from other events e.g. reflections from the vertical edge of the boulder (labelled in figure). To correct  $f_1$  amplitudes, antenna patterns were modelled for observation distance equivalent to the depth

to  $f_1$  (1.19m). Figure 8e is the FDTD derived antenna pattern predicted at  $f_1$ ; ground permittivity corresponds to that of layer 1.

### **Spreading and attenuation**

Spreading and attenuation corrections require knowing,  $r$ , the ray path length, and the attenuation coefficient  $\alpha$ . CMP data and semblance analysis yielded radar wave velocity in the propagating medium, layer thickness  $h_1$  and incidence angle ( $\theta_1$ ) which used to compute  $r$ . We then applied spreading corrections by assuming  $1/r$  spherical divergence and hence adjusting the amplitude at a given incidence angle ( $\theta_1$ ) using the ray path length corresponding to that angle.

The attenuation coefficient  $\alpha$  should ideally be estimated using site specific laboratory or field estimates of electrical conductivity. Bradford and Deeds (2006) claim that for offset to depth ratios up to 2 and  $\alpha$  in the range 0.01-0.5dB/m, the amplitude is insensitive to attenuation correction. Limestone at this field site is very resistive ( $\gg 1000\Omega\text{m}$ ) corresponding to  $\alpha$  of  $\sim 0.17\text{dB/m}$  suggesting that conductive attenuation is negligible. However, field observations show that the rock above the analyzed event is broken up, possibly due to quarrying activities; fissures will therefore contain water rendering the layer attenuative. The presence of water in the fissures could account for the higher permittivity value in layer 1 (9) relative to layer 3 (6.25). To characterize  $\alpha$  layer 1, we measured the radar quality factor  $Q^*$  (Turner and Siggins, 1994, Irving and Knight, 2003) from the CMP data using spectral ratio method, which compares the amplitude spectra of two signals recorded after different travel times. The slope of the straight line portion of a plot of  $\log_e$  [spectral ratios] versus angular frequency is proportional to  $Q^{*-1}$ . The reader is referred to the following papers for detailed explanation and theoretical basis of the method: Sears and Bonner (1981), Tonn (1991), Dasgupta and Clark (1998) and Reine et al. (2009); all applied

to seismic data and Axtell et al. (2011), for GPR application. Using the method in Axtell et al. (2011), we use the spectral ratios for  $f_1$  and  $f_0$ . Since the layers above  $f_0$  and  $f_1$  show similar permittivity values, it is assumed that attenuation in these layers will be similar and can be used to correct  $f_1$  amplitudes. Common offset wavelets (i.e. on a single trace) recorded in the CMP survey cannot be used because each wavelet has a different radiation angle and therefore a different ray path; instead, in our method, ray tracing based on Snell's law identifies traces with similar radiation angle from the surface which eliminates the need to account for antenna patterns and raypath differences when carrying out the analysis. Take off and incidence angles were limited to avoid interference from other events.  $Q^*$  values obtained range from  $18 \pm 0.4$  to  $36 \pm 0.8$  equivalent to attenuation  $0.87 \pm 0.08$  to  $0.41 \pm 0.02 \text{ m}^{-1}$  respectively. See figure 9a and 9b.

Figure 10a plots the normalized  $f_1$  AVA curve after corrections; amplitudes increase with incidence angle up to about  $25^\circ$  where a sudden decrease in amplitude occurs is inconsistent with theoretical predictions of TE thin bed reflectivity; it is rather associated with losses as a result of transmission through  $f_0$  which increase with offset. Figure 10b plots envelope amplitudes considered in this analysis and shows the region of interference from  $f_0$ . To correct for this effect,  $f_0$  transmission coefficients need to be measured, however, this is impossible due to significant interference at small offsets and also at larger offsets. At about  $40^\circ$   $f_1$  amplitude rise steadily; this can be attributed to interference from the direct wave event. For these reasons,  $f_1$  data beyond  $25^\circ$  are not considered in subsequent analysis.

## Fracture aperture and fill estimates

Fracture aperture and fill properties are constrained by finding the pair of  $\epsilon_{r2}$  and  $h_2$  which minimise the sum of squares of differences between theoretical and measured reflection amplitudes (**figure 2**). Theoretical amplitudes are computed using the broadband

model described in section 3. The fracture model comprises a thin layer (2) sandwiched between layers 1 and 3 of differing permittivity. Table 4 summarizes search parameters. The results are summarized in figures 11a and 11b. 11a shows a section of the parameter space; within which the best fit solution with the lowest rms lies. Aperture in this limit is between 0.04 to 0.05 m ( $\pm 0.001$ ), relative permittivity between 7.5 and 8.3 ( $\pm 0.1$ ) and rms between 3.9 % and 4.9 %. The ‘errors’ in both aperture and relative permittivity simply restate the sampling interval of the solution space. Low rms regions in other areas within the parameter space, correspond to fracture apertures of at least 0.1m, unlikely for a horizontal bedding plane fracture at depth: apertures observed on quarry walls are considerably smaller (figure 4b) and it would reasonably be expected that apertures at depth are narrower. Figure 12 shows field amplitudes and the best fit model with rms of 3.8 % shown in the box in figure 10; a thin layer, 0.043m thick with relative permittivity of 7.8; this could be a fracture filled with a mixture of calcite and clay or a thin limestone bed embedded within massive beds of limestone. In either case, it has posed significant contrast relative to the host rock; enough to be detected and to observe AVO characteristics.

## **Discussion**

GPR fracture AVA curves contain information on aperture and fill permittivity. In this paper, a practical approach to AVA analysis of GPR CMP data was presented. A fracture AVA curve was extracted from field data by making some simplifying assumptions and correcting amplitudes for geometric spreading, intrinsic attenuation, and antenna patterns including both transmitter radiation and receiver sensitivity wherever possible using site – specific field data as transillumination surveys on a 0.9m boulder.

We assume frequency independence, (reasonable for effective propagation of GPR signals through most rocks especially resistive ones: Annan (1996)) and horizontal layers

with homogeneous electrical properties and attenuation. The geology in our field site is limestone which appears homogeneous in outcrop except for the broken layer above  $f_0$ , which, depending on size of the fissures present, will contain varying amounts of water and consequently permittivity and attenuation. We used the  $Q^*$  value obtained from the CMP survey to correct for attenuation. Limestone bedding in the site is near horizontal with dips mostly less than  $4^\circ$ ; it is believed that these dip angles are not significant enough to affect our results. The fracture geometry was also treated as having smooth parallel walls, considered adequate as observations in the field of bedding plane surfaces shows that the surface is not significantly rough, relative to the first Fresnel zone of the radar beam: roughly 0.71m and 0.9m at  $45^\circ$  incidence. Wavelengths of the bedding plane surface roughness are in the order of 0.02m to 0.03m, small relative to the diameter of the Fresnel zone. In interpreting fracture properties we have also not taken account of effects of any possible damage zones and that of 'fracture skin' on GPR response. Thus fracture properties we obtained will represent the whole fracture system including any fracture wall properties (Tsoflias, 2004).

There are limitations to this approach associated with the GPR method itself and practical considerations. GPR is limited in terms of depth of penetration in conductive media (e.g. clay-rich soils or saturated sands) due to strong attenuation; this typically limits successful application to resistive rocks e.g. limestone and basement rocks. Another limiting factor is achieving a sufficient offset or wide incidence angle, in order to observe AVA characteristics. It is normally preferable to choose the shallowest reflections as mentioned in previous sections to avoid the need to account for transmission losses through layers above layer of interest. However with shallow reflections, it is normally difficult to access amplitude data at wider offsets (angles) due to interference from the ground wave.

## **Conclusions**

The GPR AVA method can be useful in providing qualitative information on fluid saturation/filling material and aperture. Our practical approach enabled the extraction of fracture AVA characteristics from CMP data. We presented a method of measuring antenna radiation and receiver sensitivity patterns through field transillumination surveys and validated this approach numerically. AVA analysis and the optimization method used in this analysis allow for simultaneous inversion of both aperture and fill permittivity from field data. The present study offers opportunities in various fields including hydrogeology, geotechnical and civil engineering, and also in mining practices where the detection and characterization of fractures is crucial.

## REFERENCES

- Annan A. P. 1996. Transmission Dispersion and GPR. *Journal of environmental and engineering geophysics*, **0**, pp. 125-136.
- Annan A. P., Waller W. M., Strangway D. W., Rossiter J. R., Redman J. D., and Watts R. D. 1975. The electromagnetic response of a low-loss, 2-layer, dielectric earth for horizontal electric dipole excitation. *Geophysics*, **40**, pp. 285-298.
- Axtell C., Whittaker J., Clark, R.A., Booth A., & Murray T. 2011. Measuring GPR attenuation from CMP gathers using common angle and common slowness methods. 17th European Meeting of Environmental and Engineering Geophysics of the Near Surface Geoscience Division of EAGE. Leicester, UK, 12 to 14 September 2011
- Baker G. S., Clement W. P., and Smith S. B. 1995. Amplitude and phase variations with offset in ground penetrating radar for identifying dense and light non-aqueous phase liquid contaminants, paper presented at Geological Society of America National meeting, Nov 6-9<sup>th</sup> 1995.
- Baker G. S. 1998. Applying AVO analysis to GPR data. *Geophysical Research Letters*, **25**, pp. 397-400.
- Barret E. B., Murray T., and Clark R.A. 2007. Errors in Radar CMP Velocity Estimates Due to Survey Geometry, and Their Implication for Ice Water Content Estimation. *Journal of Environmental and Engineering Geophysics*, **12**, pp. 101-111.
- Booth A., Clark R. A., and Murray T. 2010. Semblance response to a ground-penetrating radar wavelet and resulting errors in velocity analysis. *Near Surface Geophysics*, **8**, pp 235-246.
- Bradford J. H. 1998. Characterizing shallow aquifers with wave-propagation based geophysical techniques: Imaging and attribute analysis. PhD dissertation, Rice University.
- Bradford J. H., and Deeds J. D. 2006. Ground-penetrating Radar theory and application of thin-bed offset-dependent reflectivity. *Geophysics*, **71**, pp. K47-K57.

Carcione J., Botelho M., Osella A., and de la Vegas M. 2006. Fresnel reflection coefficients for GPR AVO analysis and detection of sea water and NAPL contaminants. *Near Surface Geophysics*, **71**, pp253-263

Castagna J. P. 1993. AVO analysis – Tutorial and review in: Castagna J. P and Backus M. M ed. *Offset Dependent Reflectivity – Theory and Practice of AVO analysis*. Society of Exploration Geophysicists, USA, pp. 3-36.

Dasgupta, R., and Clark R.A. 1998. Estimation of Q from surface seismic reflection data. *Geophysics*, **63**, pp. 2120-2128.

Davis J. L., and Annan A. P. 1989. Ground Penetrating Radar for High-Resolution Mapping of Soil and Rock Stratigraphy. *Geophysical Prospecting*, **37**, pp. 531-551.

Deeds J. D., and Bradford J. H. 2002. Characterization of an aquitard and direct detection of LNAPL at Hill Air Force Base using GPR AVO and migration velocity analysis. 9th International Conference on Ground Penetrating Radar, International society for Optical Engineering Proceedings, 5-19.

Deparis J., and Garambois S. 2009. On the use of dispersive APVO GPR curves for thin-bed properties estimation: Theory and application to fracture characterization. *Geophysics*, **74**, pp J1-J12.

Dix C. 1955. Seismic velocities from surface measurements. *Geophysics*, **20**, pp. 68-86.

Engheta N., Papas C., and Elachi C. 1982. Radiation patterns of interfacial dipole antennas. *Radio Science*, **17**, pp. 1557–1566.

Giannopoulos A. 2005. *GprMax2D/3D Version 2.0 User's manual*.

Grasmuek M. P. 1996. 3-D ground penetrating radar applied to fracture imaging in gneiss. *Geophysics*, **61**, pp. 1050-1064.

Gregoire C. 2001. *Fracture Characterization by ground Penetrating Radar*. PhD Thesis, KULeuven, Leuven.

Gregoire C., and Halluex L. 2002. Characterization of fractures by GPR in a mining environment. *First break: special topic – mining*, **20**, pp. 467-471.

Hafren Water, 2003. An assessment of the potential for impact on the water environment due to future mineral extraction at Threshfield Quarry, Grassington, North Yorkshire. A report prepared for Tarmac Northern Ltd Lingerfield, Knaresborough North Yorkshire.

Hollender F., and Tillard J. 1998. Modelling ground-penetrating radar propagation and reflection with the Jonscher Parameterization. *Geophysics*, **63**, pp 1993-1942.

Holliger K., and Bergman T. 1998. Accurate and efficient FDTD modelling of ground-penetrating radar antenna radiation. *Geophysical Research Letters*, **25**, pp 3883-3886.

IMC (Environmental and Geotechnical Engineering) 1996. Geological and Hydrogeological Desk Study of Threshfield Quarry, Grassington, North Yorkshire.

Innan S. U., and Innan S.A. 2000. *Electromagnetic waves*. Prentice – Hall, Inc, upper Saddle River, USA.

Irving, J. D., and Knight, R., 2003. Removal of wavelet dispersion from ground penetrating radar. *Geophysics*, **68**, pp. 960-970.

King R. W. P., and Owens M. 1992. *Lateral electromagnetic waves: Theory and applications to Communication, Geophysical prospecting and Remote sensing*. Springer-Verlag, New York.

Lane J. W., and Buursink M. L. 1999. Characterising Fractures in a bed rock outcrop using ground penetrating radar at Mirror Lake, New Hampshire. USGS Water Resources Investigation Report 99-4018C.

Lehman F. 1996. Fresnel equation for reflection and transmission at boundaries between two media with applications to georadar problems. *Proceedings of the 6<sup>th</sup> International Conference on Ground Penetrating Radar*, pp 555-560.

Michalski A., and Britton R. 1997. The Role of Bedding Fractures in the Hydrogeology of Sedimentary Bedrock – Evidence from the Newark Basin, New Jersey. *Groundwater*, **35**, pp. 318-327.

- Nelson R. A. 2001. Geologic analysis of Naturally Fractured Reservoirs; 2<sup>nd</sup> edition. Gulf Professional Publishing, Boston, USA.
- Noorishad J., Witherspoon PA., and Brekke T. L. 1971. A Method for Coupled Stress and Flow Analysis of Fractured Rock Masses. University of California, Geotechnical Eng. Pub. Pp. 71-76 128.
- Ostrander W. J. 1984. Plane-wave reflection coefficients for gas sands at non-normal angles of incidence. *Geophysics*, **49**, pp. 1637-1648.
- Priest S. D. 1993. Discontinuity analysis for rock engineering. Chapman and Hall, London.
- Radzevicius S. J., Chen C., Peters Jr. L., and Daniels J. J. 2003. Near-field dipole radiation dynamics through FDTD modelling. *Journal of Applied Geophysics*, **52**, pp75-91.
- Reine C., Van der Baan M., and Clark A. 2009. The robustness of seismic attenuation measurements using fixed- and variable-window time-frequency transforms. *Geophysics*, **74**, no. 2, pp WA123–WA135
- Reynolds J. M. 1997. An introduction to Applied and Environmental geophysics. Wiley and sons Publishers, West Sussex, England.
- Sears, E.M. and Bonner, B.P. 1981. Ultrasonic attenuation measurement by spectral ratio utilizing signal processing techniques, *IEEE Transactions on Geoscience and Remote Sensing GE-19*, **2**, pp 95-99.
- Sheriff R. E. 2002. Encyclopaedic Dictionary of Applied Geophysics. Society of Exploration Geophysicists, USA.
- Snow D. T., 1968. Rock Fracture Spacing, Openings, and Porosities. *American Society of Civil Engineers Journal: Soil Mechanics and Foundation Division*, **94** (SMA1), pp.73-91.
- Theune U., Rokosh D., Sacchi M. D., and Schmitt R. D. 2006. Mapping Fractures with GPR: A case study from Turtle Mountain. *Geophysics*, **71**, pp B139-B150.
- Tonn R. 1989. Comparison of seven methods for the computation of Q. *Physics of the Earth and Planetary Interiors*, **55**, pp 259–268.
- Tsoflias G. P., Halihan T., and Muldoon M. A. 2004. Fracture fluid flow properties investigation using GPR and Hydraulic testing methods. *Proceedings of the 10th International conference on Ground Penetrating Radar*, pp 521-524.

Turner, G. and A. Siggins, 1994. "Constant-Q attenuation of subsurface radar pulses", *Geophysics.*, **59**, pp 1192- 1200.

Valle S., Zanzi L., Sghezzi M., Lenzi G., and Friberg J. 2001. Ground Penetrating Radar Antennas: Theoretical and Experimental Directivity Functions. *IEE Transactions on Geoscience and Remote Sensing*, **39**, pp 749-758.

West, L.J., K. Handley, Y. Huang, and M. Pokar. 2003. Radar frequency dielectric dispersion in sandstone: Implications for determination of moisture and clay content. *Water Resources Research*, **39**.

Widess M. 1973. How thin is a thin bed? *Geophysics*, **38**, pp 1176-1180.

Wilson C. R., Witherspoon P.A. 1970. An Investigation of Laminar Flow in Fractured Rock. Geotechnical Report 70-6. University of California, Berkeley, p. 178.

**Table 1** CMP data acquisition parameters

Parameter	Value
Survey type/Antenna polarity	CMP /TE
Minimum/maximum offset (m)	0.37/16.05
Sampling interval (ns)	0.05
Trace increment (m)	<b>0.04</b>
Recording window (ns)	300
Stack	64
Frequency (MHz)	500

**Table 2** Inferred model of  $f_1$  showing the velocity and permittivity of the layers overlying and underlying  $f_1$  and their thicknesses.

<b>Layer</b>	<b>Velocity (m/ns)</b>	<b>Thickness (m)</b>	<b>Comments</b>
<b>1</b>	$0.102 \pm 0.00059$	1.19	Limestone
<b>2</b>	?	?	$f_1$ - Thin fracture – bedding plane
<b>3</b>	$0.122 \pm 0.0062$	1.28	Limestone

**Table 3** Boulder transillumination (antenna patterns) data acquisition parameters

Parameter	Value
Survey type/Antenna polarity	Transillumination /TE
Minimum/maximum offset (m)	0/1.98
Sampling interval (ns)	0.05
Trace increment (m)	0.02
Recording window (ns)	200
Stack	64
Frequency (MHz)	500

**Table 4** Aperture and fill permittivity estimation: search parameters

<b>Parameter</b>	<b>Value</b>	
<b>Limestone properties</b>	<b>Relative dielectric permittivity</b>	
Layer3	9	
Layer1	6	
<b>Fracture properties</b>	<b>Aperture, <math>h_2</math> (m)</b>	<b>Permittivity, <math>\epsilon_{r2}</math></b>
Lower boundary	0	1
Upper boundary	0.5	80
<b><math>\theta_i</math> at <math>f_1</math> (°)</b>	<b>9-25</b>	

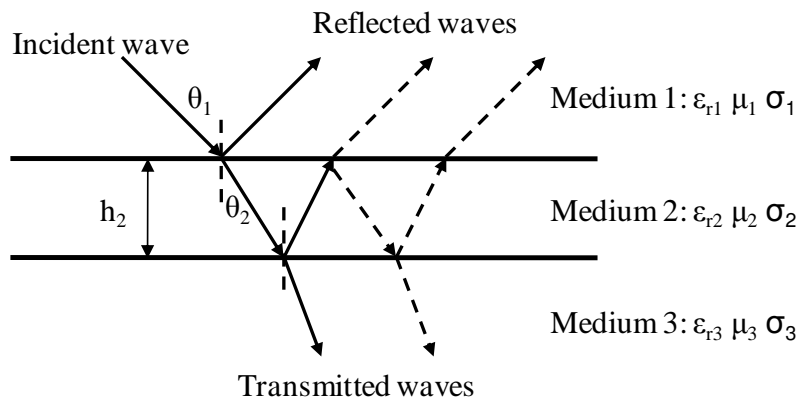


**Figure 1** Interference of multiple reflections from top and bottom surfaces defining a thin bed (medium 2) of thickness  $h_2$  embedded between 2 media (1&3).

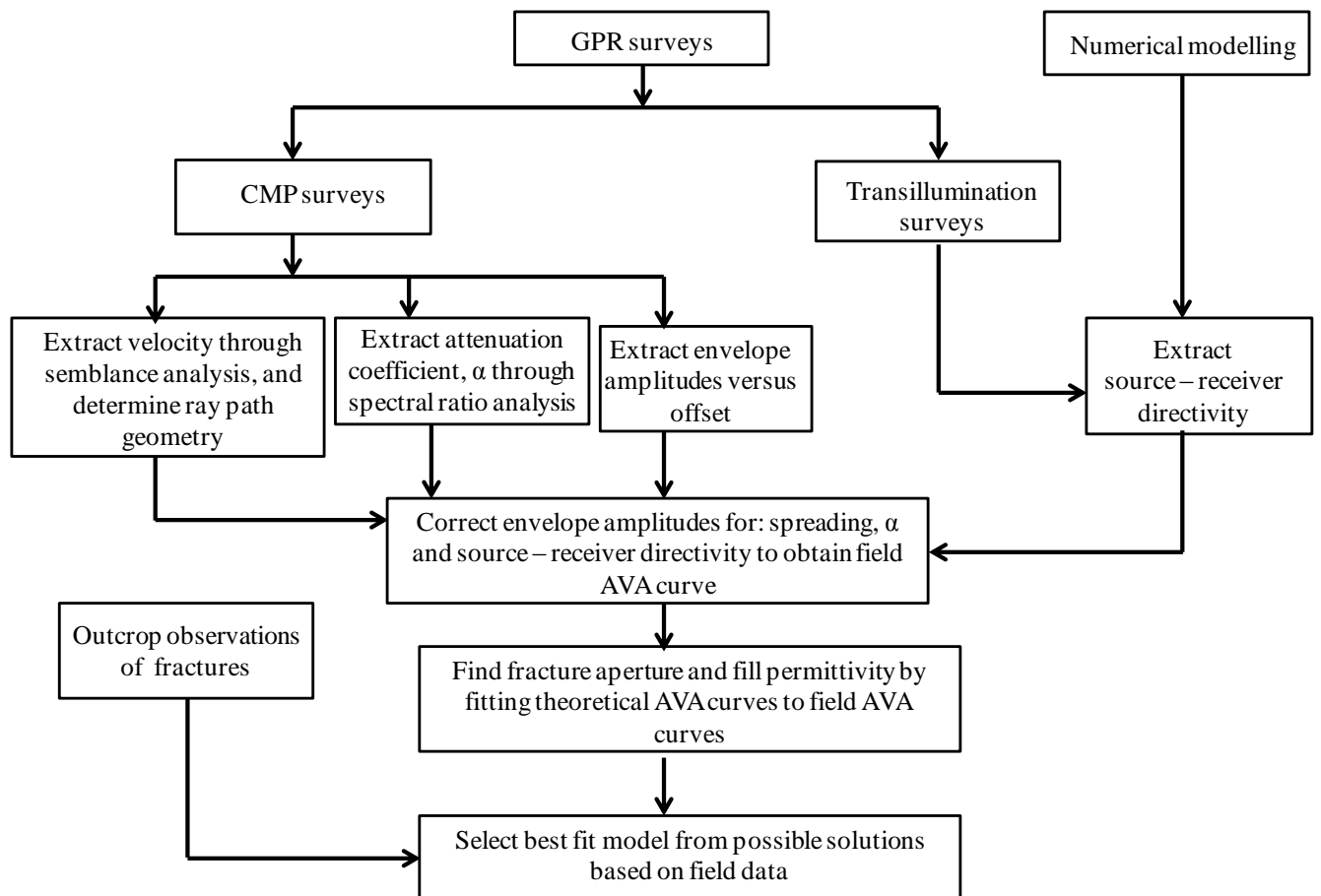
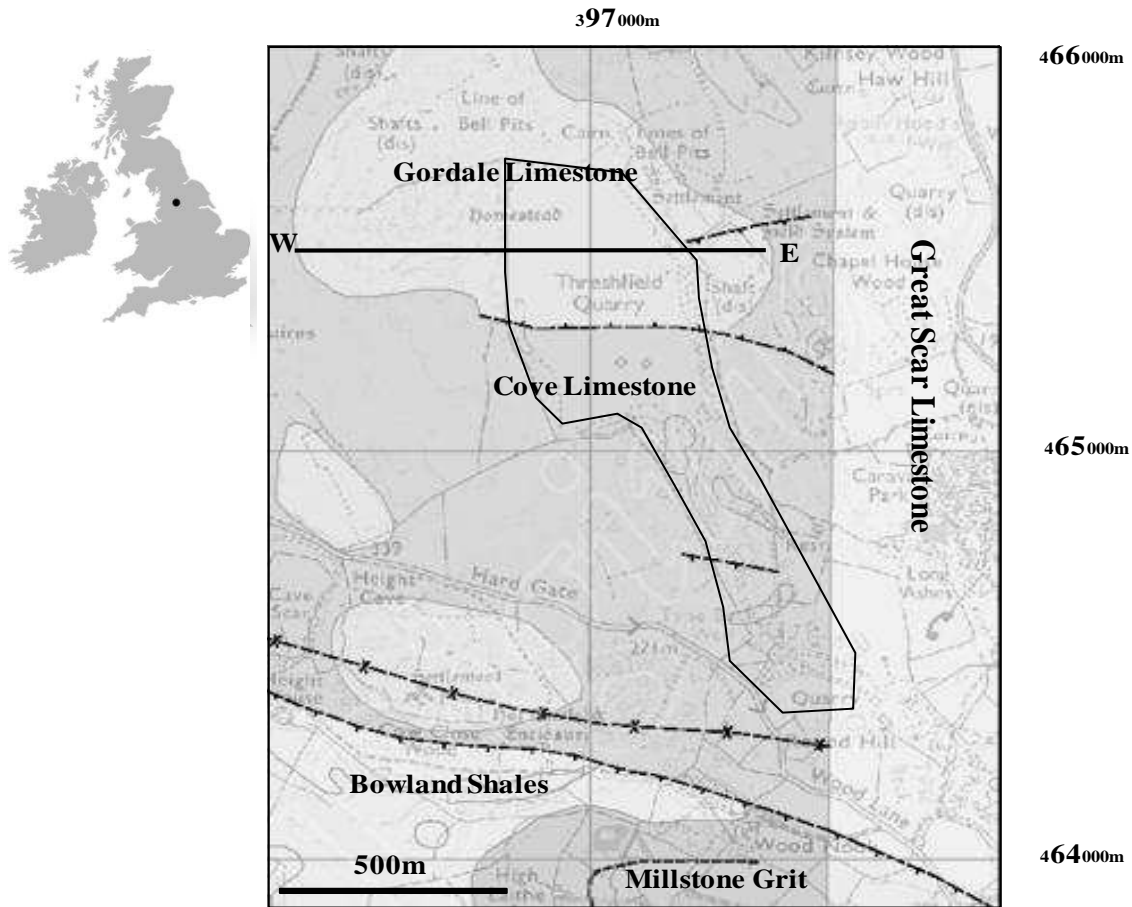


**Figure 2** A summary of the procedure, as reported in this paper, for fracture aperture and fill characterization using AVA analysis of GPR data.

(a)



(b)

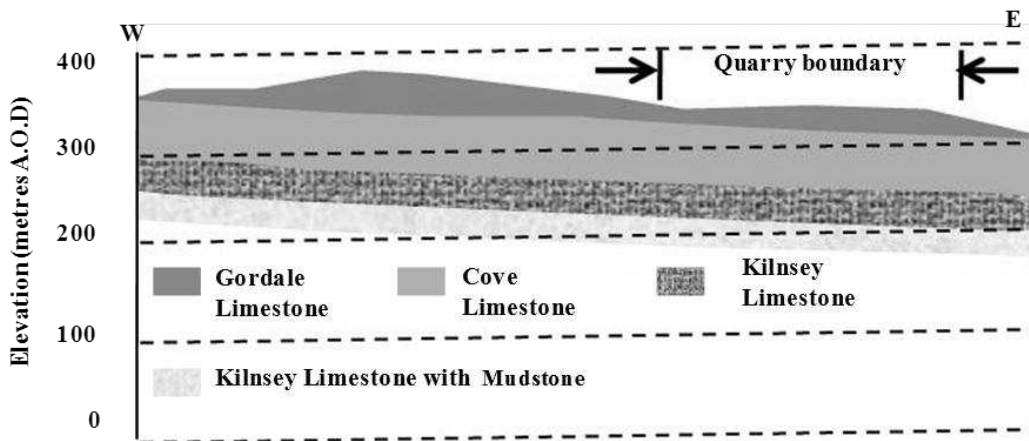


**Figure 3** (a) Location and Geology of field site; Quarry location (approximate) outlined. Modified from: Edina Digi Maps. (b) Geological cross section of line W-E in 2a modified from IMC, 1996. Co – ordinates correspond to the British National Grid Reference (NGR).

(a)



(b)

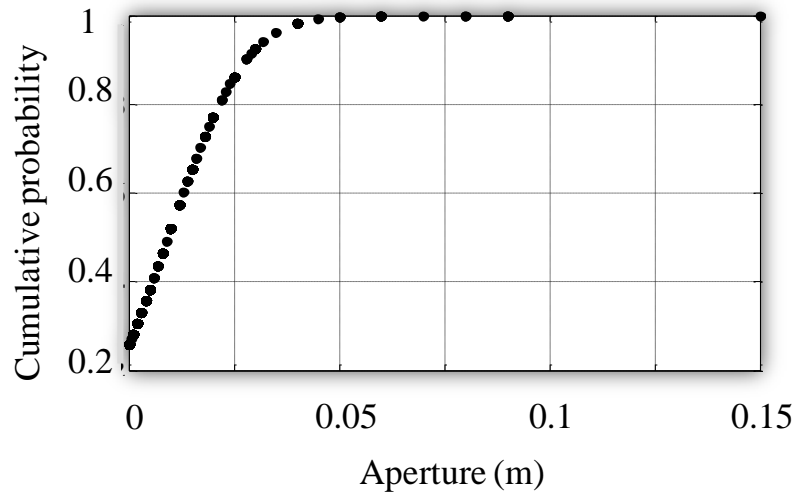
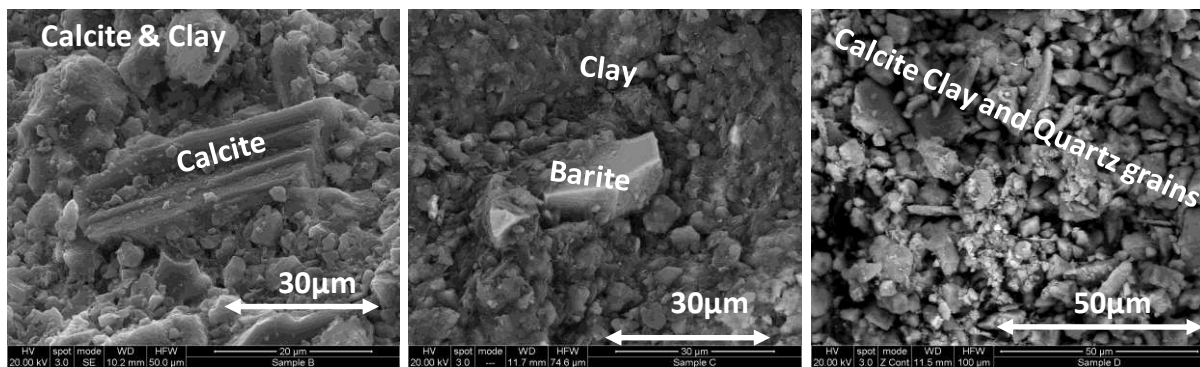


**Figure 4** (a) Quarry wall (left) and a bedding plane fracture on the same wall (right). (b) Fracture aperture distributions.

(a)



(b)

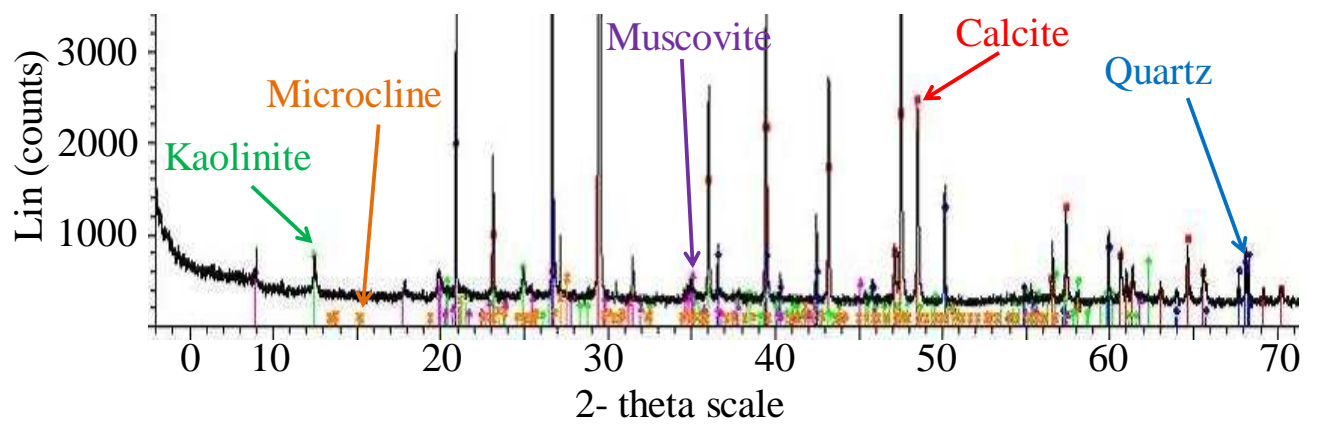


**Figure 5** (a) SEM photomicrograph of fracture fills showing minerals present. (b) XRD plot of fracture fill samples.

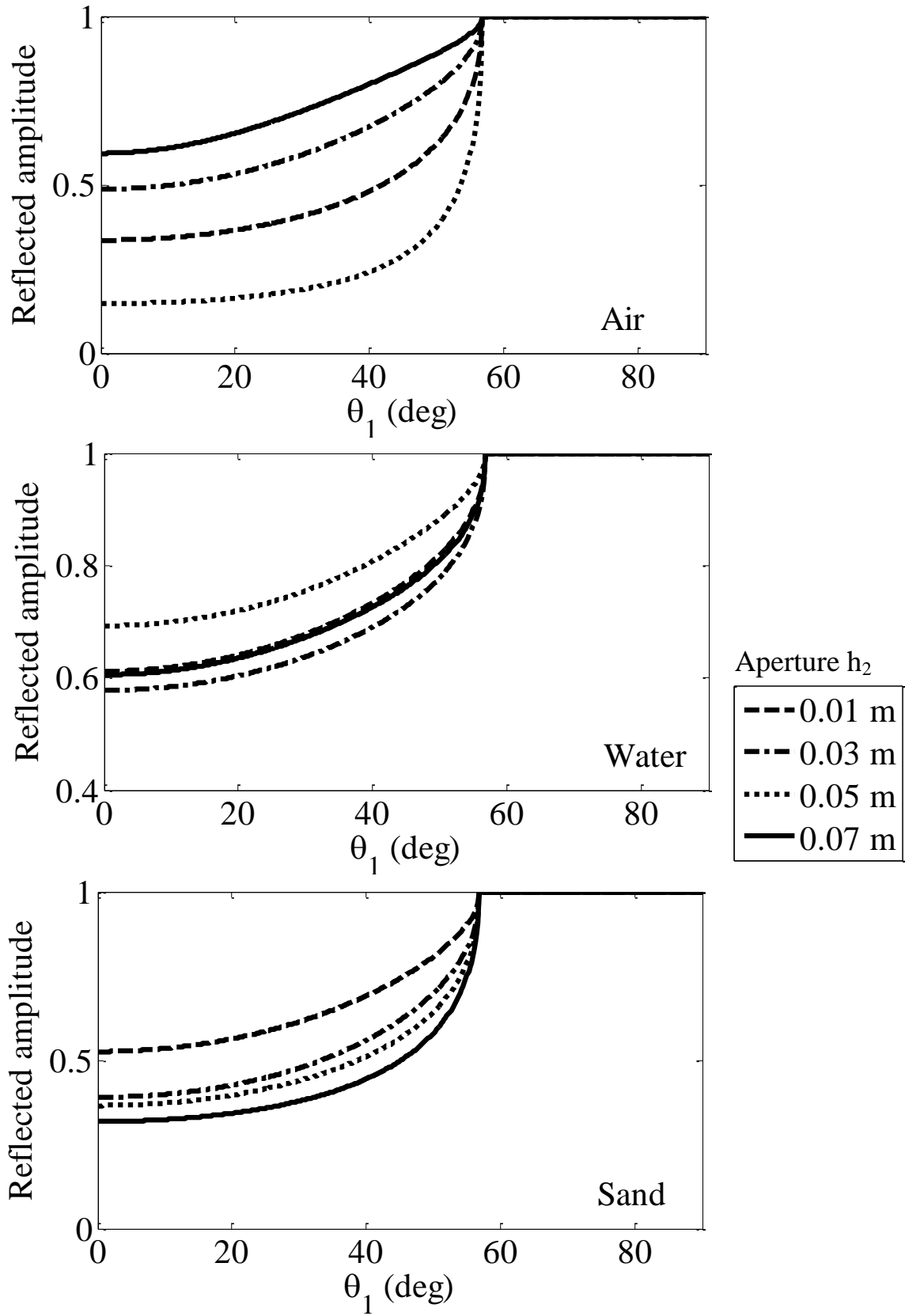


**Figure 6** Reflection amplitude of a broadband signal versus  $\theta_1$  for air, water and filled fractures in limestone ( $\epsilon_{r1} = 10$  and  $\epsilon_{r3} = 7$ ).

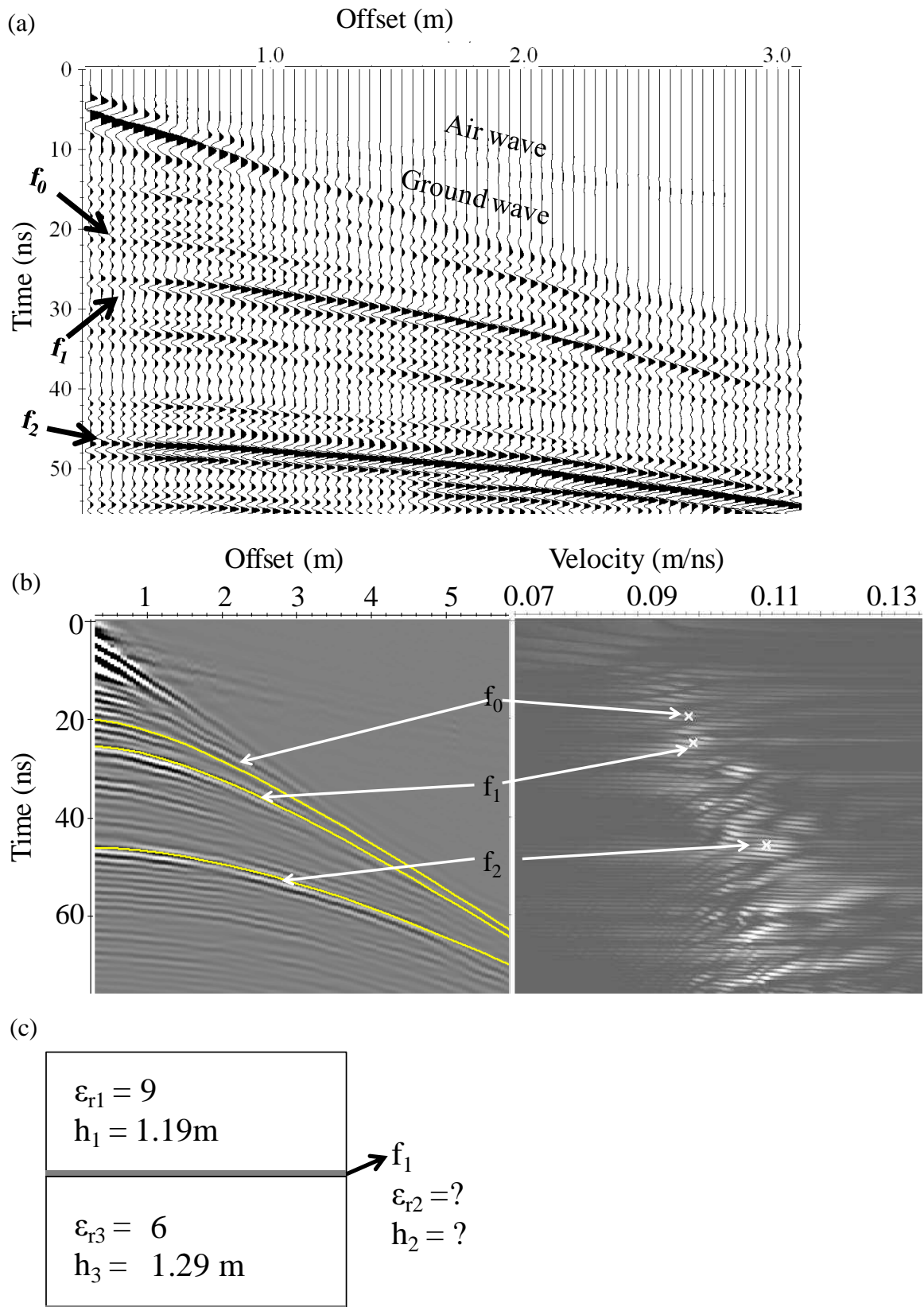


**Figure 7** (a) CMP data showing the direct air and ground waves and a series of other reflections; the studied reflection is labelled  $f_1$ . (b) Coherence display showing stacking velocities before backshifting corrections showing  $f_0 - f_2$  reflections. (c) Thin layer model for  $f_1$ ; also shown is permittivity of layers above and below  $f_1$ .

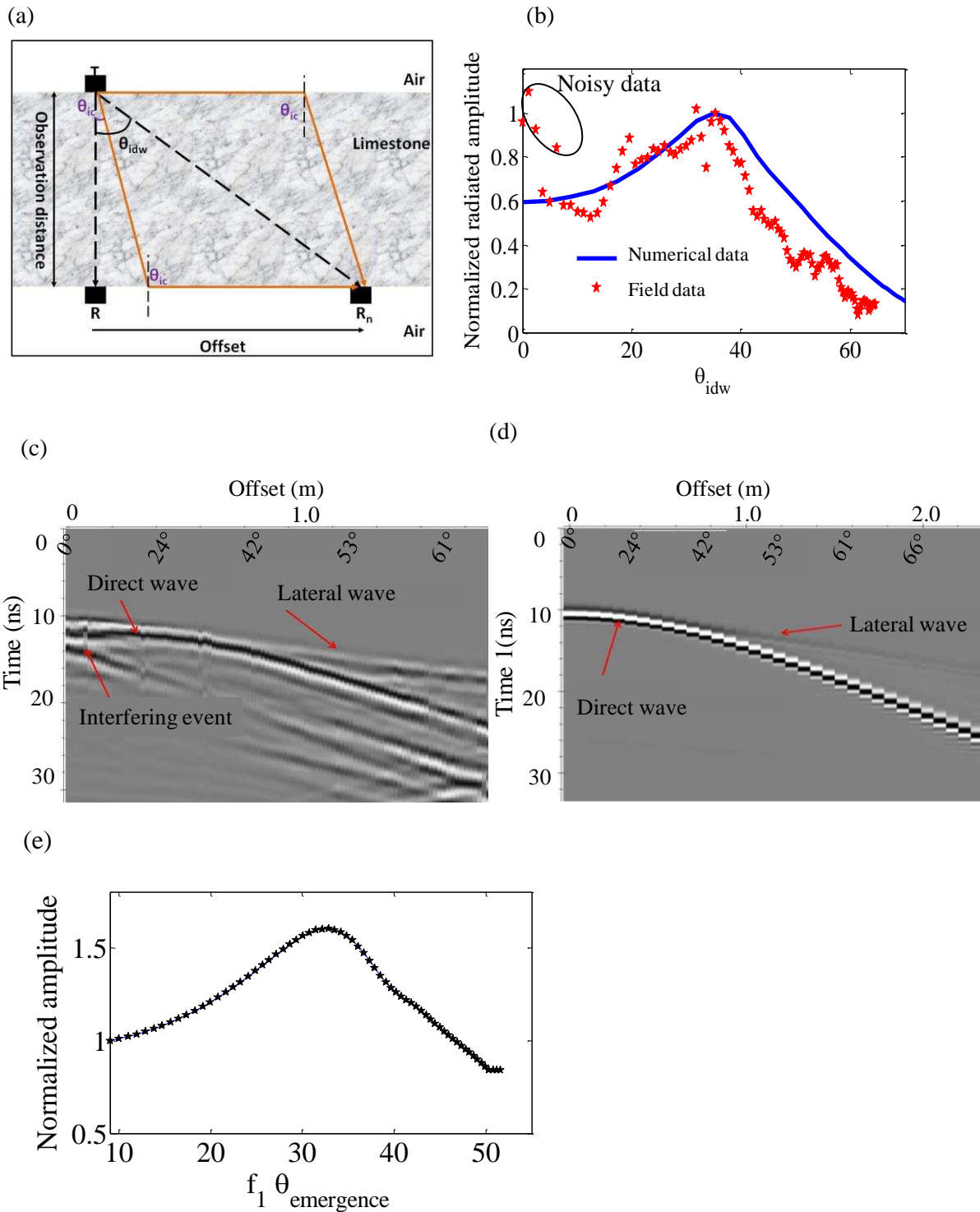


**Figure 8** (a) FDTD model geometry showing direct wave (black dashed arrows) and lateral wave (orange solid arrows) propagation paths. T and R correspond to transmitter and receiver respectively while  $\theta_{ic}$  is critical angle and  $\theta_{idw}$  is radiation angle of the direct wave. (b) Comparison between the patterns obtained from field data and numerically derived pattern at a distance of 0.9m. (c) Radargram obtained from the survey across a 0.9m thick boulder (inset), and (d), FDTD simulated radargram for the same geometry limestone ( $\epsilon_r=8$ ). (e) FDTD derived antenna pattern observed at  $f_1$ .

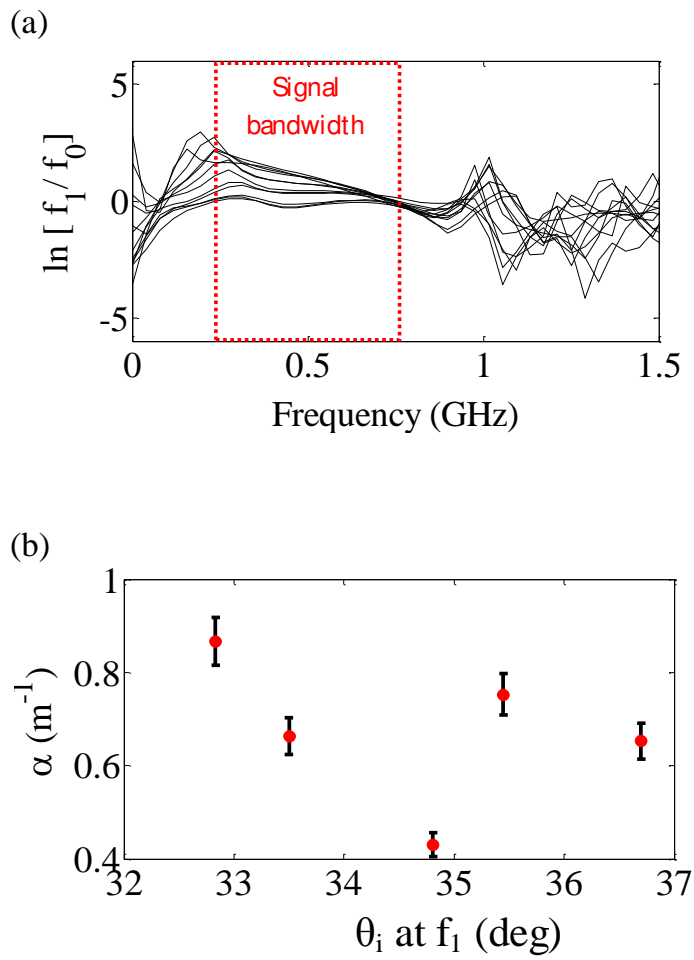
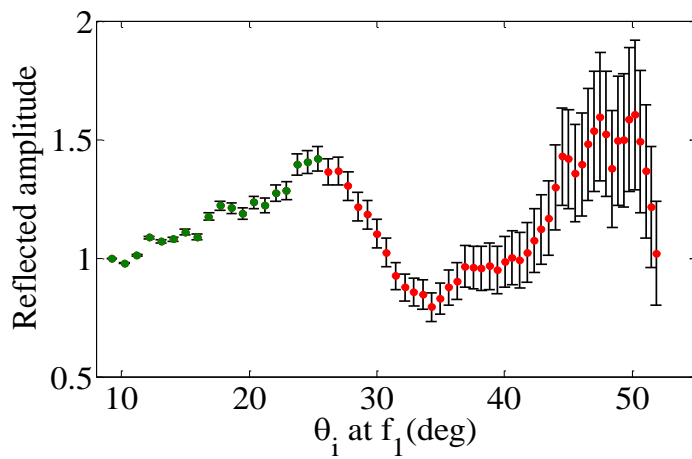


**Figure 9** (a) Spectral ratios between  $f_1$  and  $f_0$  common angle pairs. (c) Resulting attenuation values.

(a)



(b)

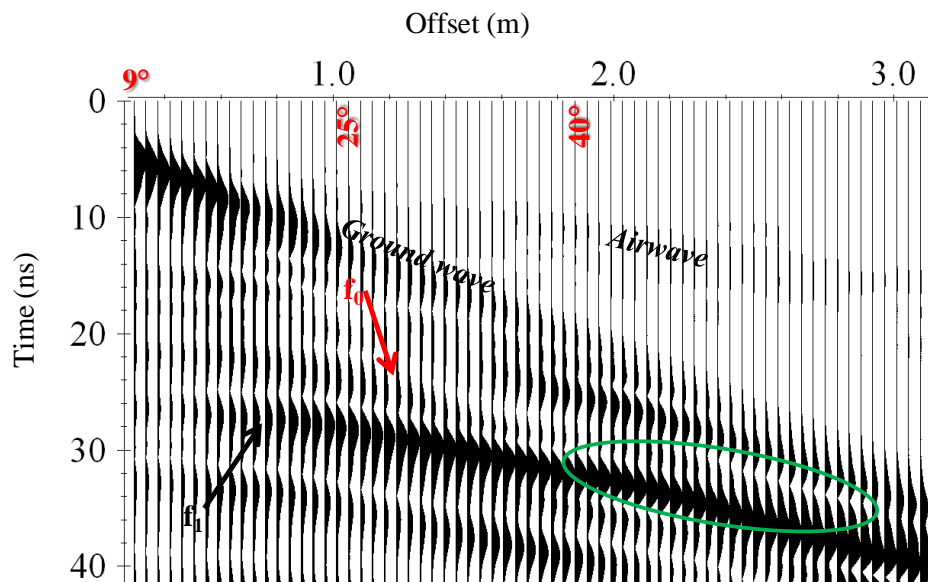


**Figure 10** (a) CMP amplitudes after spreading and antenna pattern corrections. (b) Envelope amplitudes showing  $f_0$  contributing to loss of energy beyond  $25^\circ$  (red arrow). Also shown (green circle) is the region of interference from shallow events (direct ground wave) contributing to the rise in amplitude beyond  $40^\circ$ .

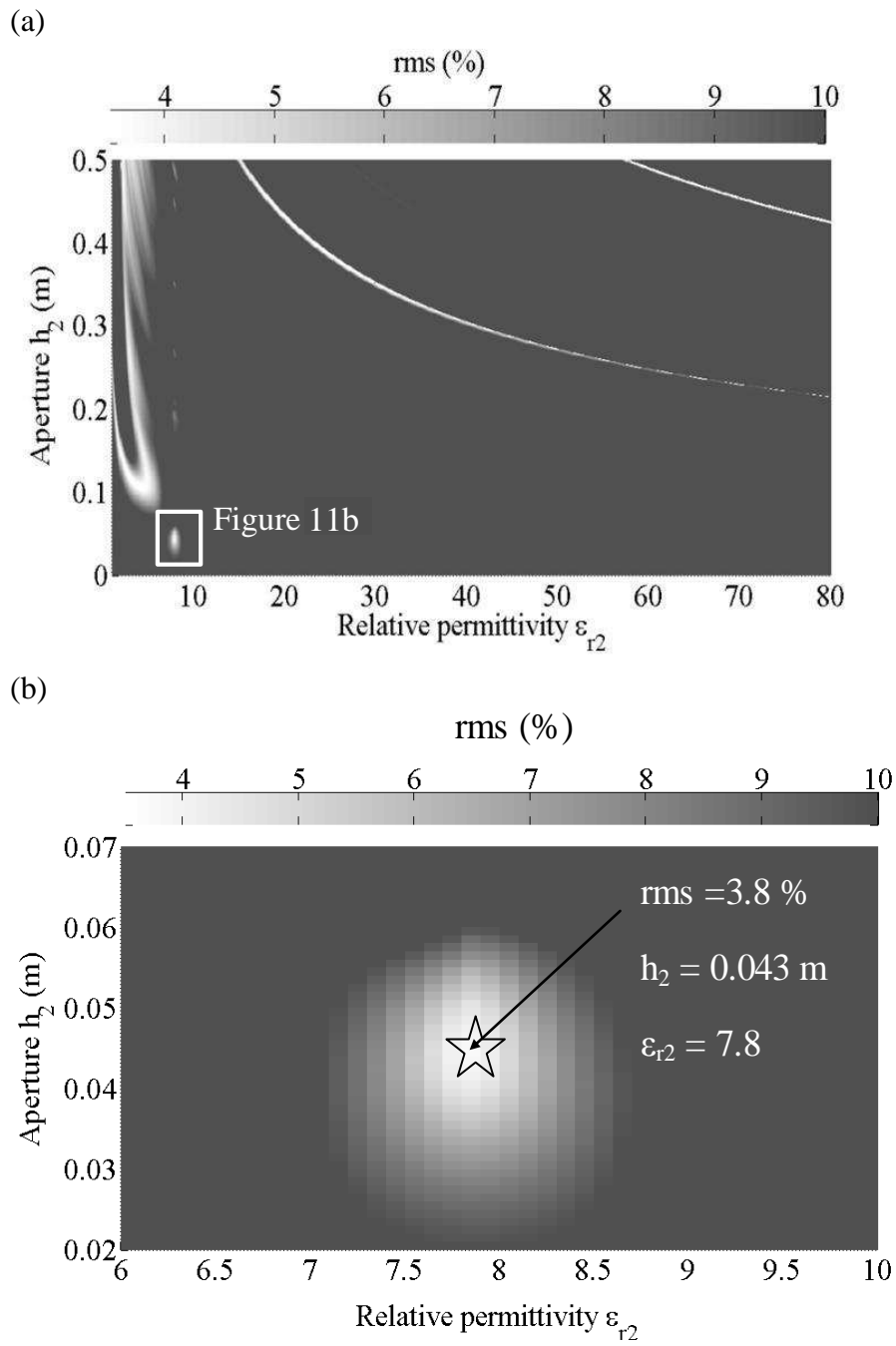


**Figure 11** Aperture and fill permittivity estimation: rms values

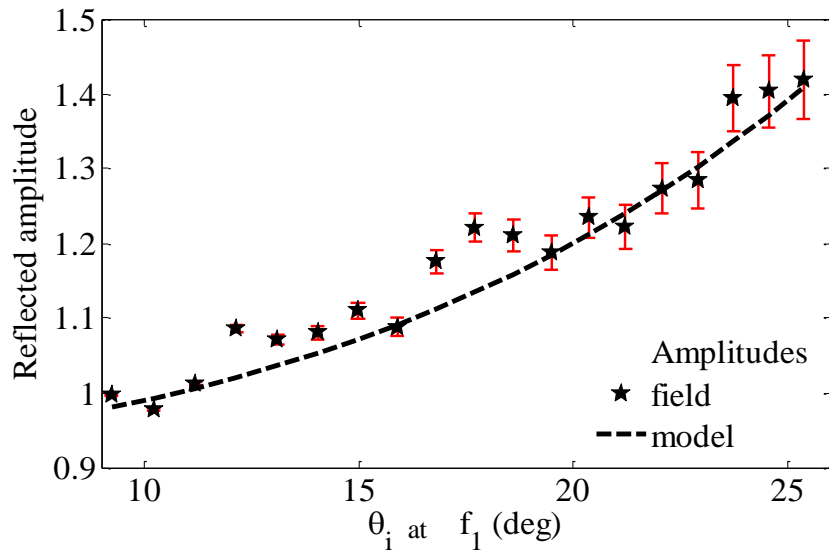


**Figure 12** Field amplitudes and a model with the least rms (3.8 %) in (b).